Materials and Design 90 (2016) 1034–1043

Contents lists available at ScienceDirect

Materials and Design

journal homepage: www.elsevier.com/locate/matdes

An artificial neural network for predicting corrosion rate and hardness of magnesium alloys

X. Xia [a,*], J.F. Nie [a], C.H.J. Davies [b], W.N. Tang [c], S.W. Xu [c], N. Birbilis [a]

[a] Department of Materials Science and Engineering, Monash University, Victoria 3800, Australia
[b] Department of Mechanical and Aerospace Engineering, Monash University, Victoria 3800, Australia
[c] Research Institute (R&D center), Baosteel Group Corporation, Shanghai 201900, PR China

ARTICLE INFO

Article history:
Received 17 April 2015
Received in revised form 27 October 2015
Accepted 9 November 2015
Available online 11 November 2015

Keywords:
Magnesium
Mg alloys
Corrosion
Neural network
Hardness

ABSTRACT

There presently exists a demand for development of magnesium (Mg) alloys for wrought applications. In this study, alloying additions of Zn, Ca, Zr, Gd and Sr to Mg were made in binary, ternary and quaternary combinations up to a maximum total alloy loading ~3 wt.%, and thus termed dilute. Such dilute alloys were studied for the purposes of potential sheet applications. The corrosion of a total of 53 custom alloys was studied in conjunction with microhardness. The results reveal that hardness increased with total alloy loading, whilst the corrosion rates did not show any clear relationship with alloy loading. Corrosion of the tested alloys was instead very sensitive to both the type and amount of the unique alloying addition. This indicates that the optimisation of properties requires a detailed knowledge of the electrochemical influence of unique alloying additions. The work contributes to an understanding of compositional effects on the corrosion of Mg, and can be exploited in prediction of corrosion resistance of existing and future Mg alloys.

1. Introduction

Magnesium (Mg) alloys continue to attract attention as engineering alloys due to their exceptional promise for reducing weight and energy usage in the automotive industry [1–3]. Of the technological issues that remain topical for the insertion of Mg components, are: (1) the inherently poor corrosion resistance of Mg alloys [4], (2) limited low temperature formability of Mg, and (3) creep resistance at elevated temperatures [5].

In this work, zinc, calcium, zirconium, gadolinium and strontium were selected as alloying elements due to their beneficial effects upon the properties of Mg. Zn is extensively used in Mg alloys as an important alloying element, which improves mechanical properties through a solid solution hardening mechanism [6] and slightly reduces the corrosion rate of Mg by decreasing the rate of anodic dissolution [7]. Ca is posited to improve the high temperature strength and creep resistance [8,9] due to the formation of high melting point intermetallic phase Mg_2Ca. Moreover, it was reported that the ternary addition of Zn in Mg–Ca alloys resulted in significant precipitation hardening in Mg–Ca–Zn alloys [10,11] at relatively low alloying concentration (1 wt% Ca and 1 wt % Zn), which was attributed to the precipitation of $Mg_6Zn_3Ca_2$ phase during isothermal ageing [11]. However, Ca has negative influence on the corrosion of Mg [12,13]. Zr has been used as a traditional grain refiner in Al-free Mg alloys, whilst the study by Gandel [14,15] indicated that Zr was detrimental to corrosion. The rare earth element, Gd, was reported to weaken the texture of Mg effectively, thus improve the formability [16,17]. The application of Sr in Mg alloys was under study because of its ability to refine the grain size [18,19] and to improve formability at low alloying levels by weakening the texture of Mg [20].

From the above point of view, the alloy composition design in this work aims to explore dilute Mg alloys as candidates for wrought applications (i.e. automotive sheet) presenting the following advantages: (1) relatively low alloying concentrations, thus the density remains low; (2) homogeneous microstructure (ideally single phase), which is beneficial for wrought processing; (3) improved strength, which may be achieved by subsequent heat treatment. The alloys produced in this work are new and not previously reported.

The corrosion resistance of multi-alloying-element dilute Mg alloys is not widely reported and thus not well understood. The focus of this study is to investigate the influence of a number of key alloying elements in various combinations on the corrosion of Mg following homogenisation treatment, with the principal focus of revealing the corrosion resistance — when alloying additions are the only variable. This study therefore contributes to elucidating the correlation between alloying and corrosion, which plays a crucial role in a systematic alloy design for achieving desired properties. However, due to the complex interactions between alloying elements in Mg alloys, it is difficult to analytically interpret the results of Mg alloys with several different alloying elements. As a result, the artificial neural network (ANN) model was recently used to manage the data in a holistic framework [13,21].

* Corresponding author.
E-mail address: xiaojian.xia@monash.eduxiaojian.xia (X. Xia).

http://dx.doi.org/10.1016/j.matdes.2015.11.040
0264-1275/

Artificial neural networks (ANN) are very useful modelling techniques based on a statistical approach. The principle of the model is to simulate the ability of human brain to recognise patterns [22,23], and if which is capable of handling complex data sets with non-linear relationships and multiple variables (i.e. ≥ 3 variables). The structure of an artificial neural network consists of three interconnected layers: an input layer; a hidden layer; and an output layer. In the hidden layer, the input data and output data is linked by the processing element (nodes or neurons) using a particular set of non-linear functions. Construction of the artificial neural network model follows the following steps: dataset collection; training of the neural network, in which the weight associated with each connection between neurons can be adjusted; and testing of the trained model.

ANN models have been employed to address multivariable problems in the corrosion-related field, as for example. Sim et al. [24] developed a neural network for prediction of supercritical CO_2 corrosion as a function of environment. Leifer et al. [25] designed an ANN model to predict pitting of Al alloy AA1100 in natural waters. Cavanaugh employed the ANN to investigate environment dependence of pit initiation [26] and pit growth [27] of Al alloy 7075-T651. Malinov [28,29] used ANN to study the correlations between processing parameters and mechanical properties and the corrosion resistance of titanium alloys.

Turning to Mg alloys, there have been a number of studies to date on the applications of ANNs as a tool to investigate and predict the corrosion properties. Kirkland [13] used an ANN to investigate the Mg–Zn–Ca alloys for the development of customised resorbable implant alloys. The corrosion rate and yield strength of Mg-RE alloys with different alloying combinations were also studied by Birbilis et al. using an ANN [21]. It was demonstrated by Willumeit et al. [30] that an ANN was useful to determine the important parameters and to predict the degradation rate of Mg under physiological conditions. Kappatos [31] successfully predicted the tensile property degradation of AZ31 alloy as a function of corrosion damage (pit depth and pitting density) due to increasing salt spray exposure time.

Apart from corrosion-related studies, ANNs were also studied as a means to investigate/predict the deformation behaviour of ZK60 Mg alloys during hot compression [32], high temperature flow behaviour of an AZ81 Mg alloy [33], the correlation between composition and mechanical properties of Mg–Al–Zn alloys [34,35], and influence of temperature on hot extrusion of AZ61 Mg alloy [36].

In this work, in order to systematically investigate the compositional effect on the corrosion of Mg, the alloys were made in binary, ternary, quaternary and quinternary additions and tested. Electrochemical experiments and microhardness test were carried out on the alloys to estimate the corrosion rate and hardness respectively. The selected testing environment is 0.1 M NaCl at room temperature, which is relevant to structural materials in practical environment. This provides a unique and new dataset for the development of an artificial neural network model for predicting the hardness and corrosion rate (principally expressed in corrosion current density), which plays a crucial role in the design of Mg alloys with desired combination of properties.

Table 1
Maximum solid solubility and respective temperature of alloying elements used in this study.

Alloying addition	Maximum solubility (wt.%)	Temperature (°C)
Zn	6.2	340
Ca	1.34	516.5
Zr	3.81	653
Gd	23.49	548
Sr	0.11	585

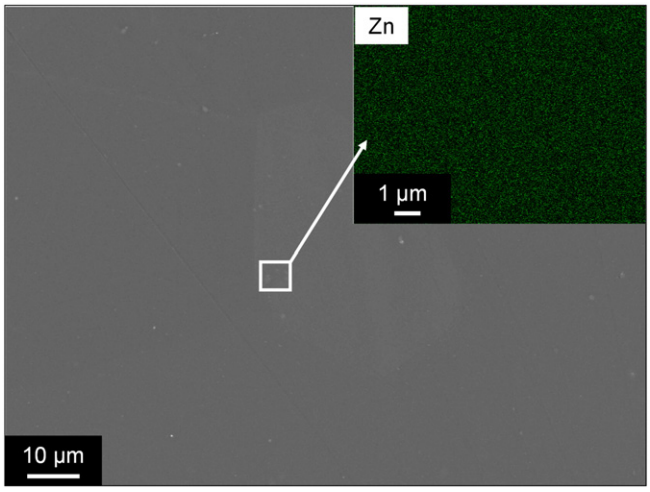

Fig. 1. Backscattered electron micrograph of the general microstructure and EDXS mapping of Mg–2Zn binary alloy.

2. Experimental methods

2.1. Materials production and processing

Mg alloys were produced in-house from 99.9% pure Mg (40 ppmw Fe), pure Zn (99.9%), pure Gd (99.9%), Mg–Zr (Mg–33Zr), Mg–Ca (Mg–27Ca) and Mg–Sr (Mg–31Sr) master alloys. The materials were melted in a graphite coated steel crucible using a vacuum induction furnace under a flowing argon atmosphere to avoid ignition of molten Mg. The alloy was melt at 720 °C for 25–30 min, vigorously stirred 5–6 times in this period. The molten alloy was then poured into a rectangular mould preheated to 200 °C, to minimise shrinkage.

Depending on the composition of the alloy, solution treatment was carried out at various temperatures for 24 h, followed by quenching in cold water. The actual compositions and temperatures of the heat treatment are given in Appendix A. The chemical compositions of alloys were confirmed via ICP-AES (Spectrometer Service Pty Ltd., Coburg, VIC, Australia).

2.2. Electrochemical testing

In order to elucidate the mechanistic aspects that dictate the ultimate corrosion rates realised (i.e. relative rates of anodic or cathodic kinetics between different alloys), the principal corrosion test method

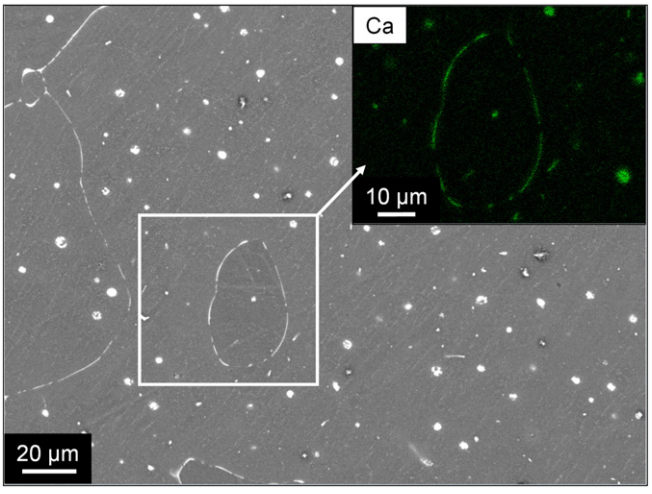

Fig. 2. Backscattered electron micrograph of the general microstructure and EDXS mapping of Mg–0.8Ca binary alloy.

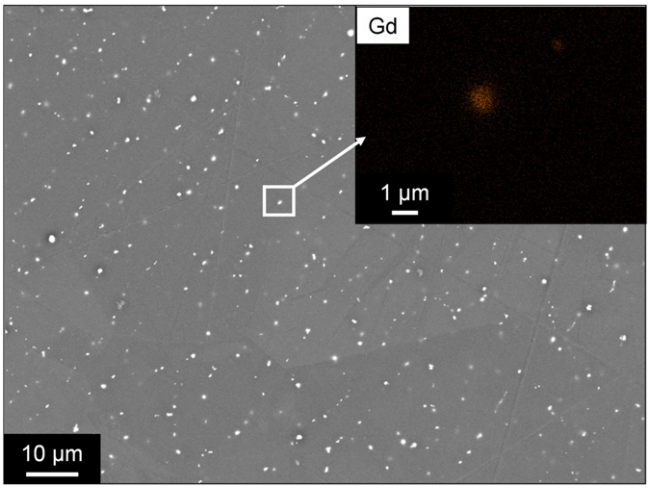

Fig. 3. Backscattered electron micrograph of the general microstructure and EDXS mapping of Mg–1Gd binary alloy.

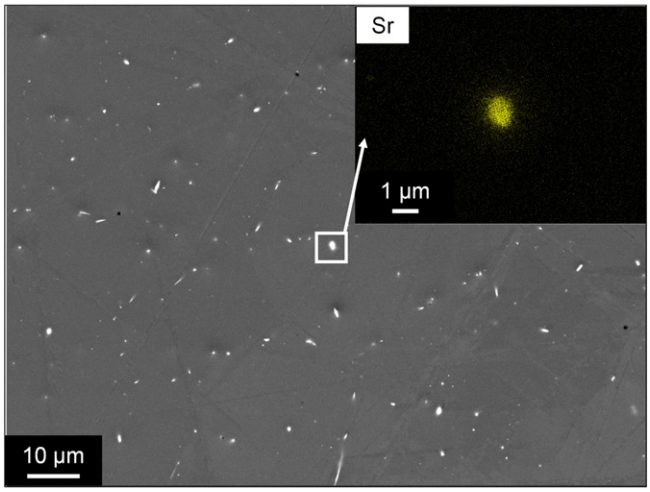

Fig. 5. Backscattered electron micrograph of the general microstructure and EDXS mapping of Mg–0.1Sr binary alloy.

reported herein is potentiodynamic polarisation. In this work, electrochemical tests were performed using a three electrode flat-cell with a working electrode area of 1 cm^2. A saturated calomel (SCE) electrode was used as the reference electrode and Pt-mesh was used as counter electrode. Potentiodynamic polarisation experiments were carried out in 0.1 M NaCl solution at 25 °C using a BioLogic VMP3 potentiostat using EC-Lab 10.02 software. Prior to each test the samples were ground to a 2000 grit SiC paper finish and conditioned for 10 min at open circuit potential to reach a stable (or very near stable) potential. The scan rate was 1 mV/s and the scan range was from −100 mV below the OCP to 500 mV above. At least 6 tests were performed on each sample. The corrosion potentials (E_{corr}) and corrosion current densities (i_{corr}) were estimated using Tafel extrapolation via EClab. It is appreciated that the potentiodynamic polarisation testing is short-term in nature, with the trade-off of being the only method capable of elucidating anodic/cathodic kinetics. In addition to potentiodynamic polarisation, a comparison with longer-term mass loss testing was also carried out, in order to provide information on the cumulative corrosion damage over a longer period.

In this study, the long-term mass loss testing was performed on Mg alloys in 0.1 M NaCl solution at room temperature. Prior to testing, the samples were ground to a 2000 grit surface finishing using SiC paper and then cleaned by sonication in ethanol. After an exposure time of 24 h, the samples were removed from the solution and dipped in a dilute (5%) nitric acid to dislodge corrosion products on the surface. Each sample was tested at least 3 times. The corrosion rate was calculated in mg/cm^2/day.

2.3. Microhardness testing

The Vickers hardness values of the alloys were tested with a 1 kg load using an automated hardness tester (Duramin A300). Prior to test, the samples were ground to a 1200 grit SiC paper finish and then cleaned with high pressure air gun and ethanol spray. A minimum of 10 separate tests were performed for each sample.

2.4. Characterisation

The microstructure and distribution of alloying elements for produced Mg alloys were characterised by the scanning electron microscopy (SEM). Prior to the characterisation, the samples were metallographically prepared to 0.05 μm finish by a silica suspension. The imaging was performed in backscattered electron mode via a JEOL JSM-7001F equipped with an energy-dispersive X-ray spectroscopy (EDXS) system.

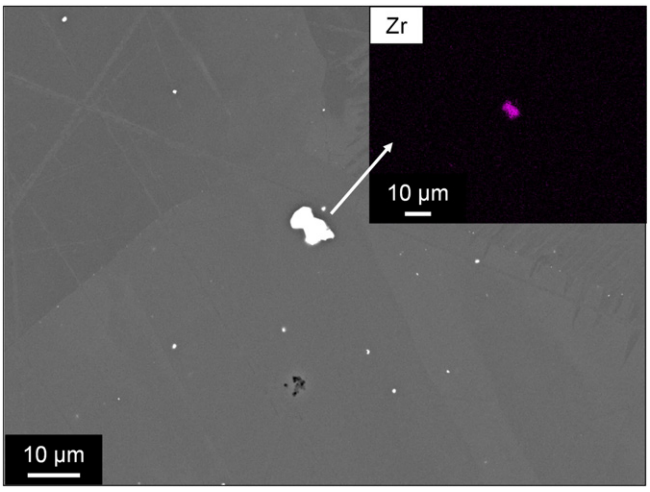

Fig. 4. Backscattered electron micrograph of the general microstructure and EDXS mapping of Mg–0.26Zr binary alloy.

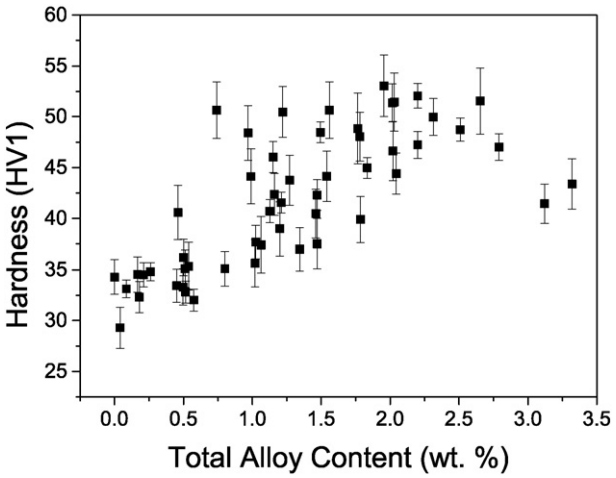

Fig. 6. Microhardness of all tested Mg alloys as a function of total alloying content.

2.5. Artificial neural network modelling

In order to study the influence of compositional variations for multi-element alloys of Mg in this work, an artificial neural network model was constructed using JMP 11 statistical software. The inputs for the model were alloying concentrations in weight percentage. The outputs of the model were the Vickers hardness values and the corrosion rate. Corrosion rate can be expressed in different forms, i.e. corrosion current density (A/cm^2), mass loss rate (g/cm^2/day) and penetration rates (mm/year). In this study, the corrosion rate is expressed in the form of corrosion current density (i_{corr}) from potentiodynamic polarisation experiments — and thus the ANN-predicted corrosion rate is expressed as a corrosion current density (A/cm^2). Prior to training, 5 datasets were randomly selected for the final independent testing of the ANNs model. 67% of the remained dataset were used for training the ANNs for microhardness and i_{corr}, and the rest was used for cross-validation.

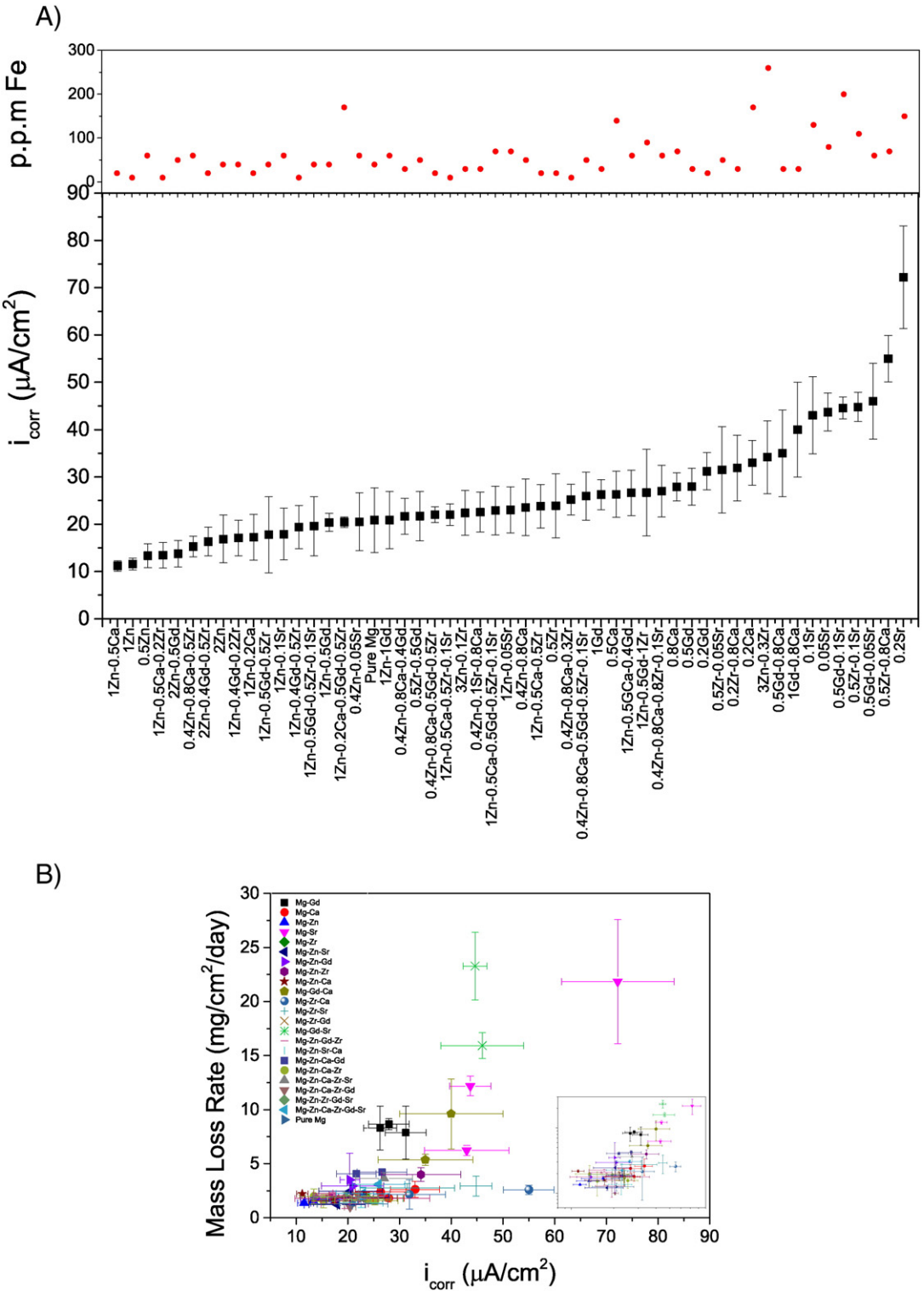

Fig. 7. (a) Corrosion current density of Mg alloys tested herein, along with corresponding Fe impurity levels in parts per million; (b) the relationship between mass loss rate and corrosion current density.

A number of neural networks with different numbers of neurons in the hidden layer were trained and tested to optimise the architecture. The artificial neural networks with the best correlations for hardness and corrosion current density are shown here. The detail of the model is shown in the relevant discussion session.

2.6. Fuzzy curve analysis

It is posited that fuzzy curves are good method for ranking the significance of input variables in neural network [37]. In this work, fuzzy curves were used for the sensitivity analysis to determine the relative significance of each input in determining the outputs.

A so-called fuzzy curve, described by Lin et al. [38], is based on the Gaussian function:

$$\varphi_{ik}(x_i) = \exp\left[-\left(\frac{x_{ik} - x_i}{b}\right)^2\right]$$

where $\varphi_{ik}(x_i)$ is the fuzzy member function corresponding to each input variable x_i, and b is typically 20% of the total range of x_i. A fuzzy curve (C_i) for each input variable x_i can be constructed by centroid defuzzification as shown below:

$$C_i(x_i) = \frac{\sum_{k=1}^{m} \varphi_{ik}(x_i) \cdot y_k}{\sum_{k=1}^{m} \varphi_{ik}(x_i)}.$$

Assuming that there are m training data sets and y_k (k = 1,2, …, m) is the output. The relative significance of each input variable (on the output) can be ranked by the range of C_i. The input variable with larger range of C_i has greater impact on the output. Prior to fuzzy curve construction, each parameter (P), inputs and outputs (i.e. composition and corresponding property value) were normalised between 0 and 1 according to:

$$P_{norm} = \frac{P_i - P_{min}}{P_{max} - P_{min}}$$

where the subscripts *norm*, *i*, *max* and *min* represent the normalised value, the *i*th dataset, the maximum value and the minimum value of the datasets respectively.

3. Results and discussion

3.1. Microstructure of Mg alloys

The maximum solid solubility limits of alloying elements used in this study and the corresponding eutectic temperatures are shown in Table 1 [39]. In this study, the alloying additions were designed to be nominally below the solid solubility limits in order to deliver a homogeneous microstructure (single or near single phase). As such, the compositional window herein is finite. The backscattered electron images of binary alloys coupled with EDXS are presented in Figs. 1-5, which allow a general insight into the microstructure of certain alloys in this study (it is not tenable to show all the microstructures).

It is noted that although all the alloying loadings were designed below their respective solid solubility limit, various intermetallic are still present after solution heat treatment, attributes to the high temperature stability and slow kinetics of dissolution of various phases. None the less, it is important to note that the volume fractions of the second phases in the studied alloys are very low or close to zero, in contrast to most existing commercial Mg alloys.

The microstructure of Mg–2Zn alloy is illustrated in Fig. 1. Owing to the relatively large maximum solid solubility (~6.2 wt.%), Zn has homogeneous distribution within the Mg matrix, without any evidence of solute segregation and individual particles.

Fig. 2 demonstrates the microstructure of Mg–0.8Ca alloy, in which both the discrete and continuous Ca-rich secondary phases with a relatively large size are observed. The secondary phases are posited to be Mg_2Ca — the only intermetallic phase in Mg–Ca binary phase diagram.

For Mg–1Gd alloy, a large amount of Gd-rich intermetallics are observed in Fig. 3. The pattern of distribution indicates that the intermetallic phases tend to locate in grain boundaries. According to the phase diagram, Mg_5Gd is the intermetallic compound in this concentration range.

The microstructure of Mg–0.26Zr is shown in Fig. 4. The detected particles are pure Zr because Zr does not form any intermetallic compound with Mg. The size of such Zr particles is relatively large.

Due to the relatively low solid solubility limit of Sr in Mg (~0.11 wt.%), Sr-containing compounds are observed in Mg–0.1Sr alloy (as shown in Fig. 5). The secondary particles with relatively small sizes are posited to be $Mg_{17}Sr_2$, which is the only compound in the relevant phase field.

3.2. Hardness of Mg alloys

The hardness as a function of the total wt.% alloy content from all the alloys tested in this study is shown in Fig. 6.

It can be seen from Fig. 6 that the hardness of Mg alloys are increased significantly as a result of alloying additions (the lowest one is ~28 HV1 and the highest one is ~55 HV1). Most results represent an overall trend that increasing total alloying loading in Mg leads to higher hardness, in a relatively monotonic manner. Nevertheless, one important observation which needs to elucidate is that the two alloys with the highest alloying concentrations (>3 wt.%) show moderate hardness (~41 HV1 and 43 HV1 respectively). On the contrary, the alloy with relatively low alloying concentrations (~0.7 wt.%) could have relatively high hardness (~51 HV1) among the alloys tested in this study. This finding indicates that the change in combination of alloying additions has great effect on the hardness of Mg alloys.

Based on the findings from Fig. 6, we note that the chemical types of the alloying additions have various impact on the hardness of Mg alloys. Because of it, it is of great importance to investigate the significance of each alloying element in hardening Mg. The sensitivity analysis in terms of hardness was performed by the fuzzy curves in the relevant session below.

3.3. Corrosion of Mg alloys

A summary of the corrosion rates expressed in corrosion current density (i_{corr}) from potentiodynamic polarisation experiments is

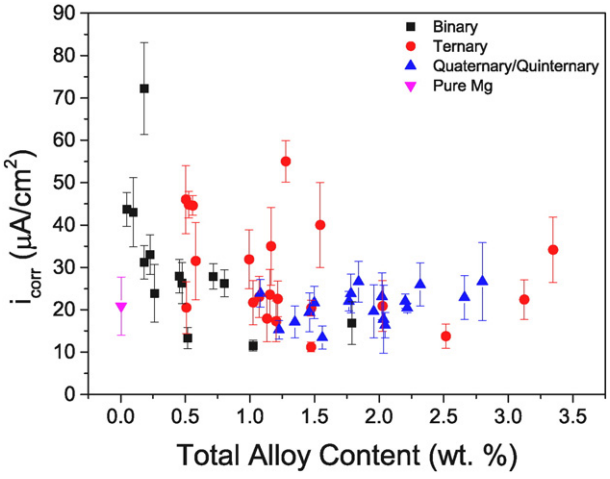

Fig. 8. Corrosion current density versus total alloy content for Mg alloys tested herein with various combinations of Zn, Ca, Zr, Gd and Sr.

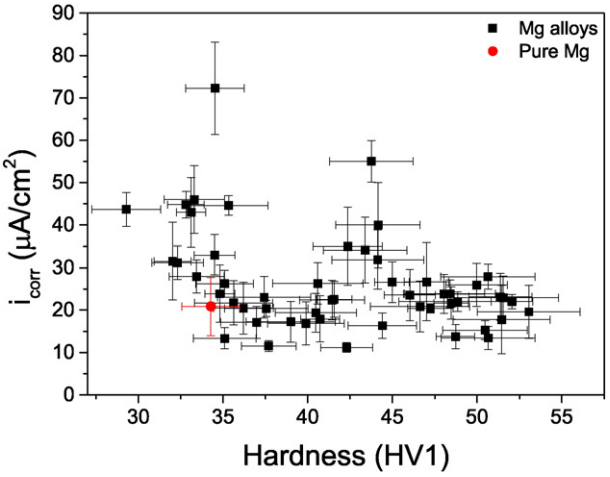

Fig. 9. The corrosion current density versus microhardness for Mg tested herein.

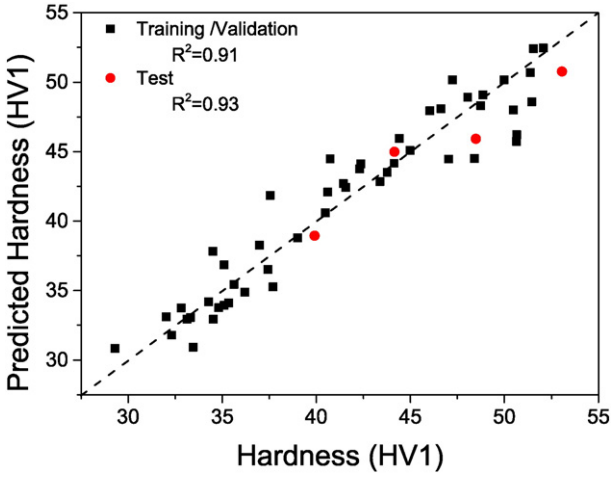

Fig. 11. ANN-predicted versus observed hardness for both the training/validation and test sets.

shown in Fig. 7 (a) and the correlation between i_{corr} and mass loss rate is shown in Fig. 7 (b). As we can see from Fig. 7 (a), it is obvious that: (1) most of the alloying additions result in higher corrosion rates than pure Mg; (2) the corrosion rates spread over a very wide range (~ one order of magnitude), indicating that Mg is very sensitive to the type and amount of alloying elements in terms of corrosion; (3) the binary and ternary alloys have relatively higher corrosion rates than quaternary and quinternary alloys; (4) the corrosion rates of quaternary and quinternary alloys are at similar levels over a range of compositions (and hardness values, as subsequently shown).

Owing to the detrimental influence of Fe on the corrosion of Mg, the corresponding impurity levels of Fe are also included in Fig. 7 (a). In this study, the Fe concentrations of most alloys are below the so-called threshold level, which is 170 ppm. [40]. Although in some alloys relatively high Fe concentrations exist, no clear relationship between corrosion rate and Fe concentration is observed in this work. It is deemed from this observation that the impurity levels of Fe do not affect the corrosion in this study.

Fig. 7(b) indicates that the corrosion rate determined by mass loss test is consistent with the results from potentiodynamic polarisation. The Mg alloys with higher corrosion current densities have higher mass loss rates.

Based on the information obtained from Fig. 7, Fig. 8 is used to visualise the influence of different alloy combinations on the corrosion of Mg. In Fig. 8, the largest spread in the i_{corr} values is seen in binary alloys, and it can be seen that the quaternary/quinternary alloys show corrosion rates within a narrow range with relatively large extent of alloy loading. Accordingly, the quaternary/quinternary alloys tested in this study seem to have higher tolerance of alloying elements without a significant change in corrosion rate.

The 'property space' for optimising properties of tested Mg alloys is investigated with the aid of Fig. 9, in which the relationship between the hardness and corrosion rate is presented. It is obvious, from a visual inspection, that the correlation between the hardness and corrosion rate is non-linear. From Fig. 9, we can see the alloying elements can reduce the corrosion of Mg slightly (lower average i_{corr}) and increases the hardness significantly (from 30 to 50). Based on the findings, we note that manipulation of alloying additions makes it possible to develop Mg alloys with high strength without much sacrifice in corrosion resistance.

3.4. *Artificial neural network model for hardness*

Given the multiple variables in composition (Zn, Ca, Zr, Gd and Sr) and large amount of data, ANN models were necessary to manage and analyse the results in a holistic way. Such a method is capable of investigating non-linear correlation and predicting the properties as a function of compositions. The ANN models employed in this study had

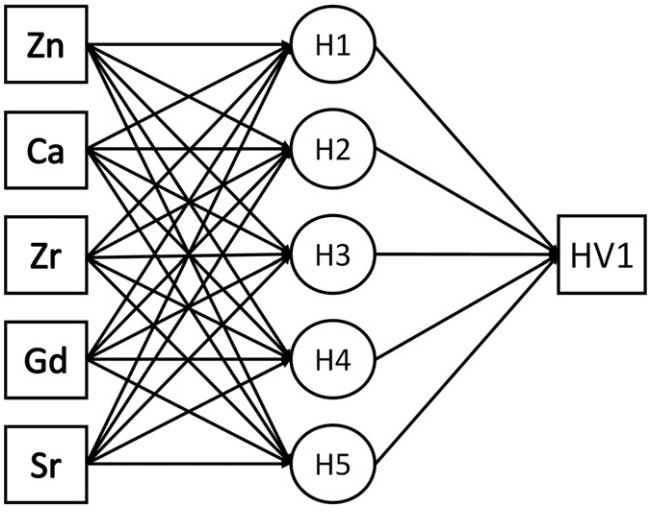

Fig. 10. ANN structure used for modelling Vickers hardness under 1 kg load.

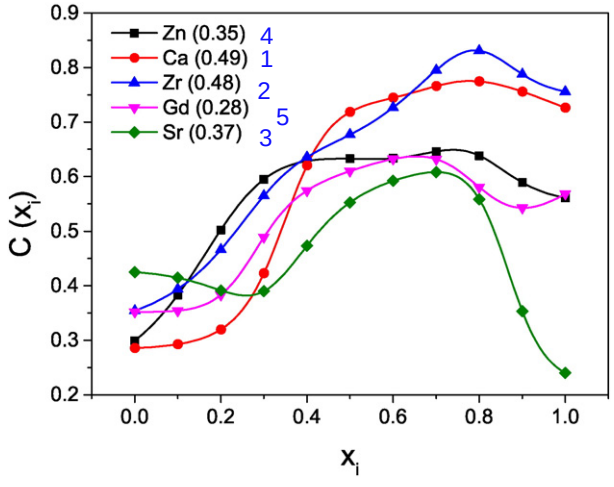

Fig. 12. Fuzzy curves for hardness, with the range of each fuzzy curve is indicated in the legend.

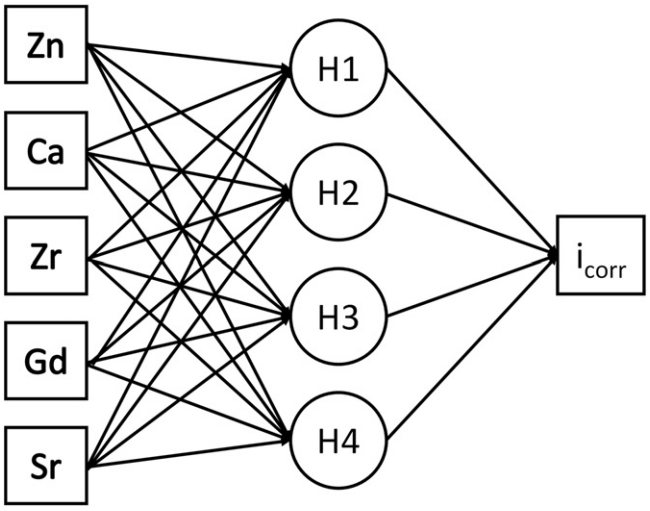

Fig. 13. ANN structure used for modelling corrosion rate expressed as corrosion current density (i_{corr}).

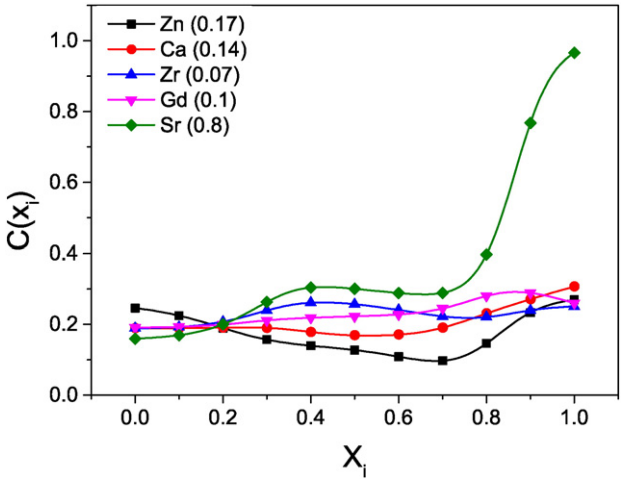

Fig. 15. Fuzzy curves for corrosion rate (i_{corr}), with the range of each fuzzy curve is indicated in the legend.

feed-forward structure, in which there is no feedback loops from outputs to inputs.

The ANN structure for hardness is illustrated in Fig. 10 and the equations for prediction are presented in Appendix B. This ANN for hardness used 5 nodes in the hidden layer to calculate the output. The ANN-predicted hardness values versus the experimental results is shown in Fig. 11. As we can see, the ANN for hardness can not only perform well in training/validation ($R^2 = 0.91$) but also accurately predict the test sets ($R^2 = 0.93$). For the prediction of hardness, this is an excellent correlation.

In order to analyse the impact of each alloying element on the alloy hardness, fuzzy curve was utilised. The fuzzy curve constructed for hardness is presented in Fig. 12 and the corresponding range of C_i of each alloying element is shown in the legend. The importance of alloying element in determining hardness is judged by the range of C_i, where the larger range is associated with the higher significance. In this study, the ranking of the alloying elements in terms of their ability to increase the hardness is Ca ≥ Zr > Sr > Zn > Gd. As shown previously in Fig. 6, it is possible to develop Mg alloys with relatively low alloying level and high hardness because the alloying additions have different impact on strength. It has been further validated by the fuzzy curves.

The constructed ANN for hardness can not only generalise the over trend in datasets well, but also predict the hardness as a function of compositions accurately.

3.5. Artificial neural network for corrosion

The structure of the ANN for corrosion is demonstrated in Fig. 13 and the equations for predicting the corrosion rate (expressed in corrosion current density, i_{corr}) as a function of compositions are shown in Appendix B. There are 4 nodes used in the hidden layer for calculation. The correlations between predicted i_{corr} and observed i_{corr} from experiments are shown in Fig. 14. It is notable that the accuracy of training/validation ($R^2 = 0.72$) and test ($R^2 = 0.87$) is relatively lower than those for hardness. However, due to the inherently chemical activity of Mg and complex interactions between alloy additions, this correlation is considerably good.

The fuzzy analysis performed in terms of corrosion rate (i_{corr}) is shown in Fig. 15 and the range of each alloying addition is indicated in the legend. Unlike the hardness where the alloying additions have monotonic positive effect, in the case of corrosion rate (i_{corr}), the effect is complex. It can be observed that Sr has extremely larger range (0.8) than the other alloying elements, which results from the relatively

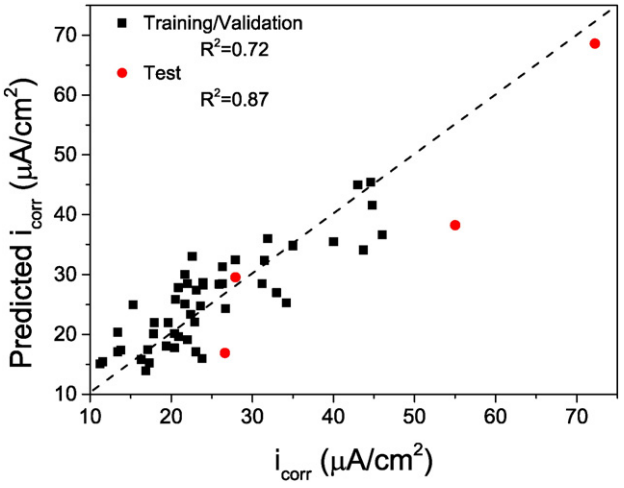

Fig. 14. ANN-predicted versus observed corrosion rate (i_{corr}) for both the training/validation and test sets.

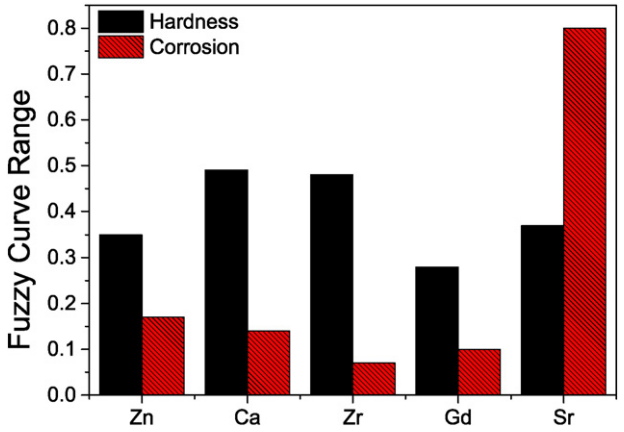

Fig. 16. An overall comparison of fuzzy curve ranges for all alloying elements, including Zn, Ca, Zr, Gd and Sr.

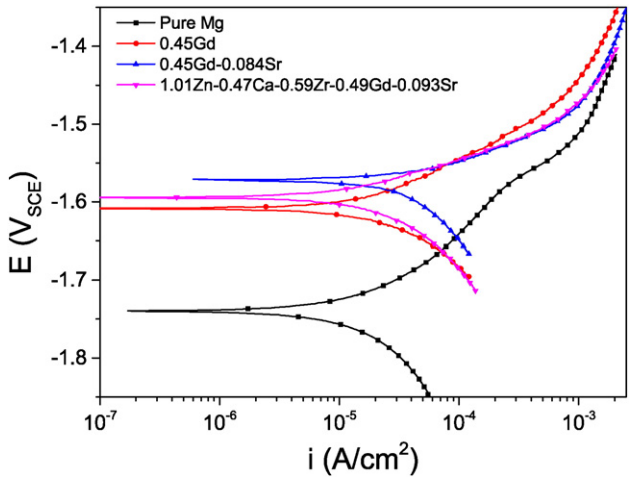

Fig. 17. Polarisation curves for pure Mg and selected binary, ternary and senary Mg alloys in 0.1 M NaCl.

low solid solubility limit of Sr in Mg (~0.11 wt.% at eutectic temperature). The range of Zr is 0.07, indicating that Zr has a minor influence on the corrosion in this study at the concentrations and combinations studied. Ca and Gd demonstrate comparative significance in determining corrosion rate. On the other hand, judging from the data collected in this study, Zn is posited to have somewhat positive influence on the corrosion (with the ternary addition of Zn, the corrosion rate is reduced, i.e. 1Zn–0.5Ca/0.5Ca, 1Zn–0.1Sr/0.1Sr). This study reveals that ANN itself can provide details in regards to mechanistic aspects and this model is capable of predicting corrosion rate (expressed in corrosion current density i_{corr}) with satisfactory accuracy within the range of compositions used in this work.

4. General discussion

The data collected in this work illustrates that alloying additions (Zn, Ca, Zr, Gd and Sr) increase the hardness of Mg. However, the magnitude of the hardness increment depends on the type and amount of alloying additions. The results show that Ca and Zr increased hardness most significantly in this study. The corrosion response of individual alloying element is relatively straightforward: (1) Ca, Zr, Gd and Sr in binary alloys increase the corrosion rate of Mg; (2) Zn in binary alloys has no obvious influence on the corrosion (slightly reduced average i_{corr}, which is still within scatters). For the alloys with quaternary and quinternary compositions, the corrosion rates are at the similar levels. This observation is consistent with the previous study on Mg-RE alloys [20], in which it was found that quaternary alloys could tolerate a greater total alloying additions than binary and ternary alloys without significant increase in i_{corr}.

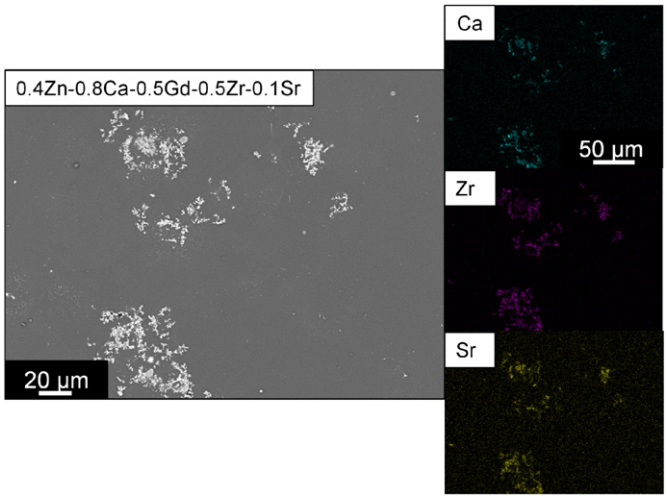

Fig. 18. Backscattered electron micrograph of the general microstructure and EDXS mapping of Mg–0.4Zn–0.8Ca–0.5Zr–0.5Gd–0.1Sr alloy.

The ANN models constructed in this study are capable of accurately predicting the hardness as a function of compositions. The correlation of predicting i_{corr} is not as high as that for hardness, however, it is still quite satisfactory owning to the complex interactions between alloying additions in terms of corrosion and the relatively large scatters in i_{corr}. The sensitivity analysis by the fuzzy curve delivers an understanding of importance of input parameters, which contributes to the capture of the key factors that dictate the outputs to optimise the composition design. In order to study the influence of each alloying element on Mg in a comprehensive way, an overall range comparison for all fuzzy curves is illustrated in Fig. 16.

It can be seen from Fig. 16, that Sr has extremely detrimental influence on the corrosion, with a moderate effect on strengthening. On the contrary, Ca and Zr have comparatively high strengthening effects and relatively low impacts on the corrosion, indicating that they can increase the hardness effectively without much deterioration of corrosion performance. Zn shows moderate significance in determining the hardness, whilst demonstrates considerable effect on reducing the i_{corr} (based on the data in Fig. 7). This analysis provides important information regarding to alloy composition design.

Artificial neural network models are often criticised because they are "statistical" models without the support of any physical theory. Because of this, a selection of polarisation curves, coupled with backscattered image is presented in Figs. 17–18 to explain the results from the electrochemical point of view and to justify the ANN model. The potential range of the polarisation curves was selected to present the respective anodic and cathodic kinetics for each alloy, and extended to a dissolution (anodic) current of >1 mA/cm^2 (which is considered to be sufficiently high to provide overall quantification of the alloy electrochemistry). It is noted that no protective films were evident for the alloys tested owing to the bulk neutral test environment.

Corrosion rate was determined by the balance of anodic and cathodic kinetics. The polarisation curve presents the relevant anodic and cathodic kinetics of Mg alloys. What is obvious from visual inspection, is that the cathodic kinetics, which represent hydrogen evolution, are increased due to the alloying additions. This is concomitant with an attendant reduction in anodic kinetics due to the alloying elements in solid solution. The net effect is corrosion rate (i_{corr}) is increased with an ennoblement of corrosion potential.

Comparison between Mg–0.45Gd and Mg–0.45Gd–0.084Sr indicates that Sr significantly enhanced the cathodic kinetics, resulting in an increase in i_{corr}, which is concomitant with an ennoblement in corrosion potential. Owing to the low solid solubility, Sr readily forms intermetallics. Accordingly, it is posited that Sr-rich intermetallics can act as cathodes to support hydrogen evolution reaction effectively, thus enhance the cathodic kinetics.

The senary (6 component) alloy has similar anodic branch with the ternary alloy, however, the cathodic branch is changed to a lower value. The possible interpretation of the reduced cathodic kinetics could be the formation of different secondary phases in this senary alloy. It can be seen from Fig. 18 that secondary phases enriched with Ca, Zr and Sr, instead of discrete Mg–Sr, Mg–Gd or Mg–Ca intermetallics, exist in the Mg–0.4Zn–0.8Ca–0.5Zr–0.5Gd–0.1Sr alloy. Based on the sensitivity analysis using the fuzzy curve, it was found Ca and Zr had relatively lower negative influence on the corrosion, whilst Sr is the most detrimental one. Because of it, Mg–Sr intermetallics is considered to sustain higher rates of cathodic reaction than Mg–Ca (Mg_2Ca) intermetallics and pure Zr. In this alloy, Sr tends to form secondary phases together with Zr and Ca instead of the formation of discrete Mg–Sr

intermetallic particles. The large fraction of cluster enriched with Ca, Zr and Sr dictates the ultimate corrosion rate.

In summary, this study revealed the compositional effect of Zn, Ca, Zr, Gd and Sr on the hardness and corrosion of Mg. Non-linear correlations between hardness and corrosion rate is found in this work. It is posited that in this study alloys with quaternary and quinternary compositions can tolerate a higher amount of alloying loading, owing to changes in the type and morphology of intermetallics. ANN models, coupled with fuzzy curves, can be used to accurately predict hardness and corrosion rate (i_{corr}). Such a predictive model is of great importance for optimising alloy development with multi-variables — but also, as shown, for unravelling the mechanistic aspects that influence properties in complex systems and large datasets.

5. Conclusions

The work presented herein has investigated the compositional effect of Zn, Ca, Zr, Gd and Sr on the hardness and corrosion of Mg, both in isolation and combination. The work has provided a large set of unreported data, which is unique on the basis of revealing the interaction between single alloying additions, as compared to more complex higher order alloy systems. In this work, it showed that the interpretation of the large database was made possible by ANN models, which can predict both the hardness and corrosion rate as a function of compositions in any given composition window (up to ~3 wt.% alloy loading in this study). The alloys studied herein represent a range of alloys that are largely solid solution alloys (or those with very little fractions of second phases) as candidates for Mg sheet. For the alloys and models tested in this study, it is shown that:

1) Alloying additions result in an increase in hardness with different significance. Ca and Zr were found to increase hardness most effectively. The former is a potent solution strengthener, the latter a grain refiner. However, on the global level, there is a general trend in the context of alloy loading and hardness for the elements and alloy loadings studied herein.
2) Corrosion rates reported were dictated by the type and amount of alloying additions present. This unequivocally indicates that chemical entity is important for corrosion. In a binary context, all of Ca, Zr, Gd and Sr increase the corrosion rate of Mg. The mechanism by which the increase is achieved is however different. Ca is more active than Mg, Gd and Sr activate the cathodic reaction, whilst Zr activates the anodic and cathodic reaction. Zn in binary did not demonstrate detrimental effect on corrosion. Among the alloys with ≥3 alloying elements, the Zn-free Mg alloys showed comparatively high corrosion rates, whilst the Zn-containing quaternary/quinternary alloys have the similar corrosion rates.
3) The ANN model presented in this study predicted the hardness and corrosion rate accurately within the tested range of compositions. Coupled with sensitivity analysis by fuzzy curves, the ANN can contribute to developing Mg alloys with a desired combination of hardness and corrosion resistance (and cost), based on the data and syntax herein.
4) Owning to the non-linear correlations between strength and corrosion rate, development of Mg alloys with high strength and a minimal increase in corrosion rate has been shown to be possible, and optimised, through quaternary and quinternary alloying additions.

Acknowledgements

The authors acknowledge the Baosteel-Australia Joint R&D Centre (BA11003) for financial support. The Monash Centre for Electron Microscopy (MCEM) is also gratefully acknowledged.

Appendix A. Composition of alloys tested in this study as determined by ICP-AES

Alloy Composition in wt.% (Fe impurity level in parts per million)							Heat treatment temperature (°C)
Zn	Ca	Zr	Gd	Sr	Fe	Mg	
0	0	0	0.18	0	20	bal.	500
0	0	0	0.45	0	30	bal.	500
0	0	0	0.8	0	30	bal.	500
0	0.21	0	0	0	170	bal.	500
0	0.46	0	0	0	140	bal.	500
0	0.71	0	0	0	70	bal.	500
0.512	0	0	0	0	60	bal.	300
1.024	0	0	0	0	10	bal.	300
1.785	0	0	0	0	40	bal.	300
0	0	0	0	0.04	80	bal.	500
0	0	0	0	0.085	130	bal.	500
0	0	0	0	0.167	150	bal.	500
0	0	0.26	0	0	20	bal.	500
0.46	0	0	0	0.041	60	bal.	500
1.02	0	0	0	0.044	70	bal.	500
1.03	0	0	0	0.096	60	bal.	500
1.01	0	0	0.46	0	40	bal.	500
1.09	0	0	0.93	0	60	bal.	500
2.07	0	0	0.44	0	50	bal.	420
3.05	0	0.07	0	0	30	bal.	420
3.04	0	0.28	0	0	260	bal.	420
1.01	0.19	0	0	0	20	bal.	500
1	0.47	0	0	0	20	bal.	500
0.42	0.73	0	0	0	50	bal.	500
0.38	0.75	0	0	0.081	30	bal.	500
0	0.8	0	0.36	0	30	bal.	500
0	0.76	0	0.78	0	30	bal.	500
0	0.79	0.2	0	0	30	bal.	500
0	0.8	0.47	0	0	70	bal.	500
0	0	0.534	0	0.041	50	bal.	500
0	0	0.43	0	0.086	110	bal.	500
0	0	0.55	0.47	0	50	bal.	500
0	0	0	0.45	0.048	60	bal.	500
0	0	0	0.454	0.084	200	bal.	500
0.986	0	0	0.358	0	40	bal.	500
0.98	0	0.14	0.34	0	10	bal.	500
1.66	0	0.006	0.378	0	20	bal.	500
0.995	0.454	0	0.385	0	60	bal.	500
0.43	0.715	0	0.35	0	30	bal.	500
0.41	0.67	0.14	0	0	60	bal.	500
0.93	0.42	0.21	0	0	10	bal.	500
0.43	0.39	0.26	0	0	10	bal.	500
0.41	0.7	0.84	0	0.066	60	bal.	500
0.41	0.71	0.57	0.51	0	20	bal.	500
0.41	0.73	0.59	0.49	0.093	50	bal.	500
0.96	0	1.27	0.56	0	90	bal.	500
1.08	0	0.47	0.48	0	40	bal.	500
1	0.2	0.5	0.5	0	170	bal.	500
1	0	0.43	0.44	0.085	40	bal.	500
1.01	0.47	0.59	0.49	0.093	70	bal.	500
1.03	0.49	0.26	0	0	20	bal.	500
1.01	0.47	0.19	0	0.095	10	bal.	500
0	0	0	0	0	40	bal.	–

Appendix B. Formulae used in ANN for corrosion rate (i_{corr}) and hardness (HV1) as a function of compositions in weight percent

$$HV1 = 45.02 + 5.27 \times H1 + 2.03 \times H2 + 3.99 \times H3 + 7.21 \times H4 + 13.97 \times H5$$

$$H1 = \tanh[0.5 \times (-4.27 + 0.81 \times Zn - 4.08 \times Ca - 2.06 \times Zr + 8.45 \times Gd + 64.77 \times Sr)]$$

$$H2 = \tanh[0.5 \times (-2.14 + 2.02 \times Zn + 4.39 \times Ca + 2.4 \times Zr - 1.15 \times Gd + 39.85 \times Sr)]$$

$$H3 = \tanh[0.5 \times (-0.77 + 9.12 \times Zn + 2.03 \times Ca - 8.91 \times Zr - 0.72 \times Gd - 2.96 \times Sr)]$$

$$H4 = \tanh[0.5 \times (-6.44 + 3.67 \times Zn + 1.28 \times Ca + 5.21 \times Zr - 6.35 \times Gd + 29.48 \times Sr)]$$

$$H5 = \tanh[0.5 \times (0.68 - 1 \times Zn + 2.01 \times Ca + 0.94 \times Zr - 2.26 \times Gd - 21.75 \times Sr)]$$

$$i_{corr} = 57.18 - 33.59 \times H1 + 46.67 \times H1 - 132 \times H3 - 47.53 \times H4$$

$$H1 = \tanh[0.5 \times (0.57 - 0.47 \times Zn - 0.76 \times Ca - 0.72 \times Zr - 0.1 \times Gd + 7.45 \times Sr)]$$

$$H2 = \tanh[0.5 \times (-1 + 0.75 \times Zn + 1.46 \times Ca + 0.67 \times Zr + 0.14 \times Gd - 14.43 \times Sr)]$$

$$H3 = \tanh[0.5 \times (-0.18 + 0.81 \times Zn + 0.065 \times Ca + 0.24 \times Zr + 0.1 \times Gd - 4.03 \times Sr)]$$

$$H5 = \tanh[0.5 \times (0.43 - 0.71 \times Zn + 1.87 \times Ca + 0.36 \times Zr - 0.27 \times Gd - 10.12 \times Sr)]$$

References

[1] M. Hakamada, T. Furuta, Y. Chino, Y. Chen, H. Kusuda, M. Mabuchi, Life cycle inventory study on magnesium alloy substitution in vehicles, Energy 32 (8) (2007) 1352–1360.
[2] A.A. Luo, Materials comparison and potential applications of magnesium in automobiles, Essential readings in magnesium technology, John Wiley & Sons 2014, pp. 25–34.
[3] T.B. Abbott, Magnesium: industrial and research developments over the last 15 years, Corrosion 71 (2) (2015) 120–127.
[4] K.U. Kainer, Magnesium alloys and technology, DGM : Wiley-VCH GmbH, Weinheim, 2003 (viii, 285 pp.).
[5] A.A. Luo, Recent magnesium alloy development for elevated temperature applications, Int. Mater. Rev. 49 (1) (2004) 13–30.
[6] H.E. Friedrich, B.L. Mordike, Magnesium technology: metallurgy, design data, automotive applications, Springer, Berlin, Heidelberg, 2006.
[7] K.U. Kainer, P. Bala Srinivasan, C. Blawert, W. Dietzel, 3.09 — corrosion of magnesium and its alloys, in: B. Cottis, M. Graham, R. Lindsay, S. Lyon, T. Richardson, D. Scantlebury, H. Stott (Eds.), Shreir's Corrosion, Elsevier, Oxford 2010, pp. 2011–2041.
[8] R. Ninomiya, T. Ojiro, K. Kubota, Improved heat-resistance of Mg–Al alloys by the Ca addition, Acta Metall. Mater. 43 (2) (1995) 669–674.
[9] Y. Terada, N. Ishimatsu, R. Sota, T. Sato, K. Ohori, Creep characteristics of Ca-added die-cast AM50 magnesium alloys, Magnesium Alloys 2003, Pts 1 and 2 2003, pp. 459–464 419–4.
[10] J.F. Nie, B.C. Muddle, Precipitation hardening of Mg–Ca(−Zn) alloys, Scr. Mater. 37 (10) (1997) 1475–1481.
[11] M. Bamberger, G. Levi, J.B. Vander Sande, Precipitation hardening in Mg–Ca–Zn alloys, Metall. Mater. Trans. A 37 (2) (2006) 481–487.
[12] A.D. Südholz, N.T. Kirkland, R.G. Buchheit, N. Birbilis, Electrochemical properties of intermetallic phases and common impurity elements in magnesium alloys, Electrochem. Solid-State Lett. 14 (2) (2011) C5–C7.
[13] N.T. Kirkland, M. Staiger, D. Nisbet, C.J. Davies, N. Birbilis, Performance-driven design of biocompatible Mg alloys, JOM 63 (6) (2011) 28–34.
[14] D.S. Gandel, M.A. Easton, M.A. Gibson, N. Birbilis, Influence of Mn and Zr on the corrosion of Al-free Mg alloys: part 2—impact of Mn and Zr on Mg alloy electrochemistry and corrosion, Corrosion 69 (8) (2013) 744–751.
[15] D.S. Gandel, M.A. Easton, M.A. Gibson, T. Abbott, N. Birbilis, The influence of zirconium additions on the corrosion of magnesium, Corros. Sci. 81 (0) (2014) 27–35.
[16] N. Stanford, D. Atwell, M.R. Barnett, The effect of Gd on the recrystallisation, texture and deformation behaviour of magnesium-based alloys, Acta Mater. 58 (20) (2010) 6773–6783.
[17] H. Yan, R. Chen, N. Zheng, J. Luo, S. Kamado, E. Han, Effects of trace Gd concentration on texture and mechanical properties of hot-rolled Mg–2Zn–xGd sheets, J. Magnes. Alloys 1 (1) (2013) 23–30.
[18] Y.C. Lee, A.K. Dahle, D.H. StJohn, The role of solute in grain refinement of magnesium, Metall. Mater. Trans. A 31 (11) (2000) 2895–2906.
[19] M. Yang, F. Pan, L. Cheng, Effects of minor Sr on as-cast microstructure and mechanical properties of ZA84 magnesium alloy, J. Mater. Eng. Perform. 19 (7) (2010) 1043–1050.
[20] A. Sadeghi, M. Pekguleryuz, Microstructure, mechanical properties and texture evolution of AZ31 alloy containing trace levels of strontium, Mater. Charact. 62 (8) (2011) 742–750.
[21] N. Birbilis, M.K. Cavanaugh, A.D. Sudholz, S.M. Zhu, M.A. Easton, M.A. Gibson, A combined neural network and mechanistic approach for the prediction of corrosion rate and yield strength of magnesium-rare earth alloys, Corros. Sci. 53 (1) (2011) 168–176.
[22] K. Gurney, An introduction to neural networks, Taylor & Francis, 2003.
[23] C.M. Bishop, Neural networks for pattern recognition, Oxford University Press, 2007.
[24] S. Sim, M.K. Cavanaugh, P. Corrigan, I.S. Cole, N. Birbilis, Aqueous corrosion testing and neural network modeling to simulate corrosion of supercritical CO_2 pipelines in the carbon capture and storage cycle, Corrosion 69 (5) (2012) 477–486.
[25] J. Leifer, J.I. Mickalonis, Prediction of aluminum pitting in natural waters via artificial neural network analysis, Corrosion 56 (6) (2000) 563–571.
[26] M.K. Cavanaugh, N. Birbilis, R.G. Buchheit, Modeling pit initiation rate as a function of environment for aluminum alloy 7075-T651, Electrochim. Acta 59 (0) (2012) 336–345.
[27] M.K. Cavanaugh, R.G. Buchheit, N. Birbilis, Modeling the environmental dependence of pit growth using neural network approaches, Corros. Sci. 52 (9) (2010) 3070–3077.
[28] S. Malinov, W. Sha, J.J. McKeown, Modelling the correlation between processing parameters and properties in titanium alloys using artificial neural network, Comput. Mater. Sci. 21 (3) (2001) 375–394.
[29] S. Malinov, W. Sha, Application of artificial neural networks for modelling correlations in titanium alloys, Mater. Sci. Eng. A 365 (1–2) (2004) 202–211.
[30] R. Willumeit, F. Feyerabend, N. Huber, Magnesium degradation as determined by artificial neural networks, Acta Biomater. 9 (10) (2013) 8722–8729.
[31] V. Kappatos, A.N. Chamos, S.G. Pantelakis, Assessment of the effect of existing corrosion on the tensile behaviour of magnesium alloy AZ31 using neural networks, Mater. Des. 31 (1) (2010) 336–342.
[32] Y.J. Qin, Q.L. Pan, Y.B. He, W.B. Li, X.Y. Liu, X. Fan, Artificial neural network modeling to evaluate and predict the deformation behavior of ZK60 magnesium alloy during hot compression, Mater. Manuf. Process. 25 (7) (2010) 539–545.
[33] O. Sabokpa, A. Zarei-Hanzaki, H.R. Abedi, N. Haghdadi, Artificial neural network modeling to predict the high temperature flow behavior of an AZ81 magnesium alloy, Mater. Des. 39 (0) (2012) 390–396.
[34] H.D. Liu, A.T. Tang, F.S. Pan, R.L. Zuo, L.Y. Wang, A model on the correlation between composition and mechanical properties of Mg–Al–Zn alloys by using artificial neural network, Materials Science Forum, Trans Tech Publ., 2005
[35] M. Krupiński, T. Tański, Prediction of mechanical properties of cast Mg–Al–Zn alloys, Arch. Mater. Sci. Eng. 56 (1) (2012) 30–36.
[36] S.H. Hsiang, J.L. Kuo, F.Y. Yang, Using artificial neural networks to investigate the influence of temperature on hot extrusion of AZ61 magnesium alloy, J. Intell. Manuf. 17 (2) (2006) 191–201.
[37] A.H. Sung, Ranking importance of input parameters of neural networks, Expert Syst. Appl. 15 (3–4) (1998) 405–411.
[38] L. Yinghua, G.A. Cunningham III, A new approach to fuzzy-neural system modeling, IEEE Trans. Fuzzy Syst. 3 (2) (1995) 190–198.
[39] A.A. Nayeb-Hashemi, J.B. Clark, ASM International, Phase diagrams of binary magnesium alloys, Monograph series on alloy phase diagrams, ASM International, Metals Park, Ohio, 1988 (ix, 370 pp.).
[40] G.L. Makar, J. Kruger, Corrosion of magnesium, Int. Mater. Rev. 38 (3) (1993) 138–153.